DUST ATTENUATION IN DISK-DOMINATED GALAXIES: EVIDENCE FOR THE 2175Å DUST FEATURE

CHARLIE CONROY¹, DAVID SCHIMINOVICH², & MICHAEL R. BLANTON³

Submitted to the Astrophysical Journal

ABSTRACT

The attenuation of starlight by interstellar dust is investigated in a sample of low redshift, disk-dominated star-forming galaxies using photometry from GALEX and SDSS. By considering broadband colors as a function of galaxy inclination we are able to confidently separate trends arising from increasing dust opacity from possible differences in stellar populations, since stellar populations do not correlate with inclination. We are thus able to make firm statements regarding the wavelength-dependent attenuation of starlight for diskdominated galaxies as a function of gas-phase metallicity and stellar mass. All commonly employed dust attenuation curves (such as the Calzetti curve for starbursts, or a power-law curve) provide poor fits to the ultraviolet colors for moderately and highly inclined galaxies. This conclusion rests on the fact that the average FUV-NUV color varies little from face-on to edge-on galaxies, while other colors such as NUV-u and u-rvary strongly with inclination. After considering a number of model variations, we are led to speculate that the presence of the strong dust extinction feature at 2175Å seen in the Milky Way (MW) extinction curve is responsible for the observed trends. If the 2175Å feature is responsible, these results would constitute the first detection of the feature in the attenuation curves of galaxies at low redshift. Independent of our interpretation, these results imply that the modeling of dust attenuation in the ultraviolet is significantly more complicated than traditionally assumed. These results also imply a very weak dependence of the FUV-NUV color on total FUV attenuation, and we conclude from this that it is extremely difficult to use only the observed UV spectral slope to infer the total UV dust attenuation, as is commonly done. We propose several simple tests that might finally identify the grain population responsible for the 2175Å feature.

Subject headings: dust, extinction — ultraviolet: galaxies — galaxies: ISM

1. INTRODUCTION

Dust is everywhere. Its obscuring and emissive signatures have been observed in environs ranging from nearby dwarf irregulars to giant ellipticals, within our own and nearby galaxies, in intergalactic space, and even in the highest redshift quasars (e.g., Trumpler 1930; Disney et al. 1989; Knapp et al. 1989; Goudfrooij et al. 1994; Zaritsky 1994; Xu & Buat 1995; Wang & Heckman 1996; Elbaz et al. 1999; Xilouris et al. 1999; Calzetti 2001; Motta et al. 2002; Wang et al. 2008; Ménard et al. 2009).

Our understanding of the composition and spatial distribution of dust in a variety of environments has increased markedly in the past decade, thanks largely to the launches of the *Spitzer Space Telescope* and the *Galaxy Evolution Explorer (GALEX)*. For example, the fraction of a galaxy's gas mass that is locked up in dust is now well-characterized as a function of galaxy mass, star formation rate (SFR), and metallicity (e.g., Draine et al. 2007; da Cunha et al. 2008, 2010). The radial distribution of gas and dust has also been extensively studied (Muñoz-Mateos et al. 2009). The importance and prevalence of polycyclic aromatic hydrocarbons (PAHs) is now widely acknowledged thanks to moderate resolution spectroscopy in the mid–IR (e.g., Leger & Puget 1984; Smith et al. 2007; O'Dowd et al. 2009).

Despite these advances, basic questions remain. It is still not known, for example, if the majority of dust forms in AGB outflows, in supernovae ejecta, or condenses directly out of the ISM (Galliano et al. 2008; Draine 2009). Computation of the dust extinction curve from first principles relies on a number of uncertain inputs, including the size, shape, and composition of the grains, and the optical constants of the constituent materials (e.g., Weingartner & Draine 2001; Draine 2003; Gordon et al. 2003; Zubko et al. 2004). A further uncertainty with broad implications for our understanding of galaxies is the relation between the stellar and dust content of galaxies; for example, how the grain size distribution varies within and between galaxies. Due to gas inflow and outflow, the stellar and gas-phase metallicities are not simply related, further compounding the problem. Without a solid theoretical understanding of the complex relation between stellar and dust content, these two components need to be modeled flexibly and independently. Despite this widely acknowledged fact, in practice a particular dust obscuration model is often simply assumed in order to then infer the underlying stellar population. Such an assumption can introduce significant biases, as we will discuss below.

The net effect of dust obscuration within a galaxy is the result of the combination of the underlying dust extinction curve, geometry, and radiative transfer. Here, geometry is taken to mean not only the large–scale distribution of dust with respect to the stars, but also the local geometry, which includes the clumpiness of the interstellar medium (ISM). Geometrical effects can make the relation between the underlying extinction curve and the resulting attenuation curve (which measures the net loss of photons within a galaxy) arbitrarily complicated (e.g., Natta & Panagia 1984; Witt et al. 1992; Calzetti et al. 1994; Witt & Gordon 1996; Városi & Dwek 1999; Witt & Gordon 2000; Granato et al. 2000; Charlot & Fall 2000; Pierini et al. 2004; Tuffs et al. 2004; Panuzzo et al. 2007). For example, a clumpy ISM, aris-

Department of Astrophysical Sciences, Princeton University, Princeton, NJ, USA

² Department of Astronomy, Columbia University, New York, NY, USA
³ Center for Cosmology and Particle Physics, New York University, New York, NY, USA

ing for example from turbulence, will result in an attenuation curve that is greyer than the extinction curve.

When the optical depth approaches unity, the effects of geometry become especially important. In such cases, the light measured in the blue/ultraviolet may not trace the same regions of the galaxy as the red/near–IR light. Consider a disk galaxy viewed edge—on that is optically thick in the UV and optically thin in the near-IR. The ultraviolet light emitted from the far side of the galaxy will be heavily extinguished, and so the ultraviolet light collected by an observer will be preferentially sampling the near side of the galaxy. In contrast, the near–IR will more faithfully trace the entire stellar population because the galaxy is relatively transparent in this wavelength range. These effects are rarely considered when modeling the SEDs of galaxies.

If we knew the underlying, unobscured stellar population, the ratio between the intrinsic and observed light would then provide a direct measure of the attenuation. Unfortunately, it is not possible to know unambiguously the underlying stellar population. Less direct methods are therefore required. For example, the attenuation curve can be estimated in a sample of galaxies with similar stellar populations and variable amounts of dust. In such cases, ratios between more and less heavily attenuated spectra can provide estimates of the net attenuation curve in the sample. Such a technique was utilized by Calzetti et al. (1994) in order to probe the average attenuation curve of starburst galaxies. The Balmer decrement was used as an estimator for the amount of dust attenuation, and, with the assumption that the galaxies in their sample were of similar metallicity and SFR, the average attenuation properties were estimated.

Similar techniques for probing the wavelength–dependent attenuation have recently been applied by Johnson et al. (2007a,b) to photometry of a large sample of low redshift galaxies, Conroy (2010) who analyzed the restframe UV photometry of star–forming galaxies at $z \sim 1$, and Noll et al. (2009) who analyzed spectra of star–forming galaxies at $z \sim 2$. In the present work we follow in this vein by considering the colors of disk–dominated galaxies as a function of their inclination. Since inclination will correlate with dust attenuation but not with stellar populations, comparing less to more inclined systems allows us to isolate the effects of increasing dust opacity on the observed properties of galaxies (e.g., Giovanelli et al. 1994, 1995; Masters et al. 2003; Driver et al. 2007; Unterborn & Ryden 2008; Maller et al. 2009; Masters et al. 2010; Yip et al. 2010).

Another constraint on the attenuation curve comes from the relation between the ratio of total infrared to UV luminosity and UV spectral slope $(L_{\text{TIR}}/L_{\text{UV}} - \beta)$, or the 'IRXβ' relation). Star-forming galaxies with redder UV spectra tend to have higher IRX. It is widely believed that this relation is primarily a sequence in dust attenuation (e.g., Kong et al. 2004). Various recipes have thus been proposed to use the IRX- β relation to estimate the total UV attenuation based on the observed UV spectral slope (e.g., Buat et al. 2005; Burgarella et al. 2005; Cortese et al. 2008). This relation is of particular importance to the study of high-redshift galaxies, where only restframe UV and optical photons can be readily collected for large samples of galaxies (although significant samples at $z \sim 1-2$ with restframe IR data are growing rapidly, e.g., Reddy et al. 2006; Salim et al. 2009; Reddy et al. 2010). For most studies of high redshift galaxies, the observed UV slope, β , is used in conjunction with a locally estimated IRX $-\beta$ relation to estimate the dust opacity.

This approach is essential, for example, to interpret recent observations of galaxies at $z \approx 6-8$ (e.g., Bouwens et al. 2009).

The IRX $-\beta$ relation is different for starbursts (Meurer et al. 1999) and normal star–forming galaxies (Dale et al. 2007; Boissier et al. 2007), and in addition depends somewhat on the star formation history (Kong et al. 2004; Johnson et al. 2007b; Muñoz-Mateos et al. 2009), $60\mu m$ luminosity (Takeuchi et al. 2010), bolometric luminosity (Reddy et al. 2006), and the star–dust geometry (Panuzzo et al. 2007). These dependencies result in substantial scatter in the IRX $-\beta$ plane, which, in conjunction with the fact that the IRX $-\beta$ is nearly vertical over much of the relevant parameter space (i.e., IRX varies considerably over a relatively narrow range in β), calls its utility into question (Bell 2002).

The most prominent feature of the MW extinction curve is the strong, broad dust feature at 2175Å, the 'UV bump' (Stecher 1965). This feature is also seen, albeit more weakly, along most sightlines in the LMC and along one of the five sightlines probed in the SMC (Gordon et al. 2003). It is also seen along sightlines in M31 (Bianchi et al. 1996). There are now confident detections of this feature in the extinction curves of more distant galaxies as well, as probed by background gamma ray bursts and quasars, and gravitational lenses (Elíasdóttir et al. 2009; Motta et al. 2002; Wang et al. 2004; Mediavilla et al. 2005), Puzzlingly, there are many examples of galaxies that do not show this feature in their extinction curve (e.g., York et al. 2006; Stratta et al. 2007). The carrier of this extinction feature is not known, although owing to its strength it must be due to some abundant material, such as carbon. Measurements of the grain albedo suggest that the feature is not due to scattering (see data compilations in Witt & Gordon 2000; Draine 2003). Several dust models associate this feature with PAH absorption (e.g., Weingartner & Draine 2001) although there are other possibilities (Draine & Malhotra 1993, e.g.,).

Understanding the prevalence of the UV bump in the attenuation curves of other galaxies is essential for broadband photometric studies of galaxies. For example, at $z\sim 0$ the UV bump falls into the *GALEX* NUV-band, at $z\sim 1$ it falls within the *B*-band, and at $z\sim 2$ it redshifts into the *R*-band. If present in the attenuation curves of galaxies, the UV bump would therefore result in substantially more, and likely more uncertain, attenuation in particular filters at particular redshifts.

Based on spectra from the *International Ultraviolet Explorer*, Calzetti et al. found an average attenuation curve for starburst galaxies that lacked a UV bump. The absence of a UV bump in the starburst attenuation curve led Witt & Gordon (2000) to suggest that in such galaxies the underlying dust extinction curve lacks a UV bump. A detailed analysis of the ultraviolet through infrared photometry of M51 revealed little evidence for a UV bump within individual HII regions (Calzetti et al. 2005). Conroy (2010) also found no evidence for a UV bump as strong as that seen in the MW in star–forming galaxies at $z \sim 1$. In stark contrast, Noll et al. (2009) presented strong evidence for a UV bump in stacked restframe UV spectra of $z \sim 2$ star–forming galaxies. Finally, Capak et al. (2009) presented tantalizing evidence for a strong UV bump in at least one $z \sim 7$ galaxy.

Thus, while the UV bump appears to be a ubiquitous feature of the MW and LMC extinction curves, there is little evidence for this feature in the net attenuation curves of other galaxies. However, it is important to recognize that a systematic inves-

tigation of the UV attenuation in $z\sim 0$ 'normal' star-forming galaxies is currently lacking. While the effects of geometry and scattering can diminish the strength of the UV bump with respect to the underlying extinction curve, it is a generic prediction of radiative transfer calculations that if the UV bump is present in the extinction curve, its presence will be detectable in the resulting attenuation curve (Witt & Gordon 2000; Panuzzo et al. 2007). Given the observations of the UV bump in the extinction curves of other galaxies, the attenuation curves of at least some galaxies should show a UV bump, even if the strength of the bump is weak. This expectation serves as motivation for the present study.

There is currently no clear picture linking together these various observations. One possibility is that the radiation field modulates the strength of the UV bump, as suggested by Gordon et al. (2003). The typical radiation field in the SMC and the local starburst galaxy sample is much harsher than the MW, potentially explaining why a UV bump is not seen in such systems. It would be hard to explain the results of Noll et al. in this context, however, given that their sample is dominated by high SFR systems. Granato et al. (2000) explained the result from Calzetti et al. as being due to the fact that the UV energy production in starbursts is dominated by young stars that are heavily embedded within molecular clouds. In their model, attenuation in starbursts is therefore governed by the wavelength-dependent fraction of UV photons produced by young stars (whose light is heavily extinguished by their birth cloud). These authors predicted that the attenuation suffered by 'normal' star-forming galaxies would show evidence of a UV bump because in this case significant UV energy is provided by intermediate age stars that have left their birth clouds. Such stars will suffer attenuation primary from the diffuse dust, where significant 2175Å absorption may be expected. It is not immediately obvious whether or not this explanation can accommodate the results from Noll et al. Draine et al. (2007) has recently demonstrated a deficiency of PAH emission in the infrared in galaxies with low gas-phase metallicities (see also Engelbracht et al. 2005; Smith et al. 2007). Metallicity may therefore play an important role.

In the present work we investigate the wavelengthdependent attenuation by dust for a sample of disk-dominated galaxies. Our sample is carefully selected to be homogeneous and complete. We then consider the ultraviolet, optical, and near-infrared colors as a function of inclination. Since inclination will only correlate with dust attenuation and not physical parameters such as star formation nor metallicity, the inclination-dependent colors will provide a robust and sensitive probe of the wavelength-dependent attenuation in disk-dominated systems. This technique is therefore similar in spirit to that of Calzetti et al. (1994, 2000), although for a sample of 'normal' star-forming galaxies, and utilizing photometry rather than spectroscopy. Averaging the flux of many galaxies considerably simplifies the modeling of the underlying stellar population because the average star formation history (SFH) of many normal galaxies must be smooth. By normal here we mean galaxies not chosen to have special SFHs, such as starburst or post-starburst galaxies. We will focus especially on the attenuation properties in the NUV band, and will therefore be able to make strong statements regarding the presence of the UV bump in the average attenuation curve of normal star-forming galaxies.

Where necessary, a flat Λ CDM cosmology with $(\Omega_m, \Omega_{\Lambda}) =$

(0.30, 0.70) is adopted, along with a Hubble constant of $H_0 = 100h$ km s⁻¹ Mpc⁻¹. All magnitudes are in the AB system (Oke & Gunn 1983). A Chabrier (2003) initial stellar mass function (IMF) is adopted when quoting stellar masses.

2. DATA

Redshifts, coordinates, ugriz photometry, and structural properties are derived from Sloan Digital Sky Survey (SDSS; York et al. 2000) data, as made available through the NYU Value Added Galaxy Catalog⁴ (VAGC; Blanton et al. 2005). We do not simply use the photometry from the SDSS catalogs, because the automated pipeline often incorrectly deblends large galaxies. In addition, the images themselves are generally over-subtracted due to the sky estimation procedure, which uses a median smoothed field in 100" by 100" boxes (Blanton et al. 2005). In order to address these issues, Blanton et al. (in prep) measure the smooth sky background from heavily masked versions of each imaging run. In this way, we avoid subtracting away light from large galaxies. Blanton et al. (in prep) have implemented a de-blending pipeline similar to that described by Lupton et al. (2001), but with parameters optimized for brighter and larger objects. For small objects these measurements agree well in general with the original SDSS catalog values; for larger objects (half-light radii > 10'') our galaxy measurements tend to be brighter in flux and larger in size.

We use the 'lowz' VAGC sample, which is constructed from the SDSS Data Release 6 (Adelman-McCarthy et al. 2008), but with the photometric re-reductions discussed above. This sample includes all galaxies with redshifts z < 0.05. Sersic (1968) profile fits have been made to the radial light profiles of galaxies in this sample (the profile fits were corrected for seeing). We will make use of the Sersic index n, where recall that n = 1 corresponds to an exponential light profile and n = 4 corresponds to a de Vaucouleurs profile. We will also make use of the axial ratio, b/a, where b and a are the semi-minor and semi-major axes, respectively. The axial ratio is measured within a radius containing 90% of the total light, and will be taken to be a proxy for the galaxy inclination. Petrosian magnitudes are used herein.

Gas-phase oxygen abundances have been estimated from the SDSS spectra by Tremonti et al. (2004), although these measurements are only available for galaxies in the SDSS Data Release 4. When considering galaxies split according to gas-phase metallicities, we will only use galaxies that are in the Tremonti et al. catalog.

Near–IR photometry are provided by the Two Micron All Sky Survey (2MASS Jarrett et al. 2000). We make use of the K–band only in Figure 1 when investigating the properties of our sample, and so make no attempt to perform matched aperture photometry on the 2MASS data.

The *GALEX* survey (Martin et al. 2005) is providing ultraviolet imaging in the FUV and NUV filters (with effective wavelengths of 1539Å and 2316Å, respectively). In order to accurately probe the UV through optical SED of galaxies as a function of inclination, we have re-measured *GALEX* photometry self-consistently for our sample by computing magnitudes within the Petrosian aperture defined by the SDSS photometry (Petrosian magnitudes in SDSS are defined according to the Petrosian radius, r_P , measured in the r-band). Our photometry was performed on *GALEX* images that have been calibrated and background subtracted. Thus, the FUV, NUV,

⁴ http://sdss.physics.nyu.edu/vagc/

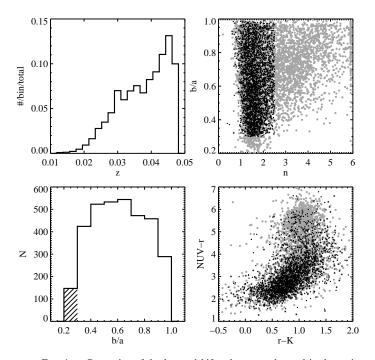


FIG. 1.— Properties of the low redshift galaxy sample used in the main analysis. Upper left: Redshift distribution normalized to the total number of objects in the sample. Upper right: Relation between Sersic index n and axial ratio b/a for the full low redshift sample (randomly diluted by 60% for clarity; grey symbols), compared to the subsample used in the main analysis (black symbols). Lower left: Histogram of axis ratios for the sample used in the main analysis. Bin widths are 0.1, starting at b/a = 0.2, which corresponds exactly to the bins used in later sections. The hatched bin is excluded from our analysis for reasons discussed in the text. Lower right: Color—color diagram (symbols are as in the upper right panel). UV—optical—near-IR colors have been shown to efficiently separate truly quiescent from dusty star—forming galaxies. The galaxies used in this sample populate the latter locus

and ugriz magnitudes are all measured through the exact same aperture. The Petrosian aperture (which is defined as $2r_P$) is much larger than the half–light radius and so differences in the PSF between GALEX and SDSS should have a negligible effect on the derived photometry, especially for the exponential light profiles that dominate our sample. Zero points for the FUV and NUV magnitudes are adopted from Morrissey et al. (2007).

E(B-V) reddening estimates are derived from Schlegel et al. (1998) via the utilities in the kcorrect v4.1.4 software package (Blanton & Roweis 2007). Photometry is corrected for Galactic extinction using E(B-V) and the MW extinction curve of Cardelli et al. (1989). In particular, we use the following values for $R_i \equiv A_i/E(B-V)$, where A_i is the extinction in magnitudes for filter i: 8.29, 8.18, 5.16, 3.79, 2.75, 2.09, 1.48, and 0.30 for the FUV, NUV, ugriz, and K bands.

K-corrections are estimated with the routines made available in the kcorrect v4.1.4 package. The SDSS ugriz photometry is used as input to estimate k-corrections for both the SDSS photometry and GALEX photometry. Photometry is k-corrected to z=0.04, which is the median redshift of the sample. Typical k-corrections are of order 0.01 magnitudes and therefore have no significant effect on our results; they are included merely for completeness.

The kcorrect v4.1.4 package also provides estimates of the stellar masses of galaxies given a set of input photom-

etry. We have used the SDSS photometry to estimate stellar masses for our sample, assuming a Chabrier (2003) initial mass function. We prefer to use photometry for stellar mass estimation because masses derived in this way are only weakly dependent on galaxy inclination (stellar masses differ by < 0.1 dex between highly inclined and face—on systems; Maller et al. 2009). Other, popular stellar mass estimators based on spectroscopy (Kauffmann et al. 2003; Tojeiro et al. 2009), suffer stronger dependencies with inclination, which indicates a systematic source of bias in the masses.

Our goal is to explore the inclination-dependent dust characteristics of a uniform sample of disk-dominated galaxies. In order to construct such a sample we select galaxies with n < 2.5 to separate disk-dominated from bulge-dominated galaxies. In addition, galaxies are selected in a narrow stellar mass range $9.5 < \log(M/M_{\odot}) < 10.0$ in order to define a homogeneous and volume-limited sample. Mass and SFR are correlated at $z \sim 0$ (e.g., Brinchmann et al. 2004; Salim et al. 2007) and so our selection on mass may be interpreted roughly as a selection on SFR as well. Galaxies at z < 0.01 are removed from our sample, as they are generally very large on the sky and thus accurate photometry is complicated. We also remove 112 galaxies with $r_P < 4$ ", as inclination measurements become unreliable for such small galaxies because of seeing (see below). With these cuts we are left with 3394 galaxies with detections in all GALEX and SDSS filters. This is our fiducial sample.

As discussed in Masters et al. (2003), the effects of seeing can bias inclination measurements for galaxies with small angular sizes. The bias manifests itself as a deficiency of small, highly inclined objects. Indeed, our sample shows such a deficiency for galaxies with $r_P \lesssim 8$ ". The median Petrosian radius of our fiducial sample is 8".4, so this bias potentially affects a significant fraction of our sample with high inclinations. However, we have re-computed all of the results in following sections only including galaxies with $r_P > 8$ " (and widening the stellar mass cut to $9.25 < \log(M/M_{\odot}) <$ 10.0 in order to increase the sample size), and find that the inclination-dependent colors change by an inconsequential amount. Moreover, these issues primarily affect galaxies with 0.2 < b/a < 0.3 and since we consider only galaxies with b/a > 0.3 we can be confident that our results are robust to seeing biases.

Several properties of our fiducial sample are shown in Figure 1, including the redshift distribution, scatter plot of inclination and Sersic index, distribution of inclinations, and a color–color plot. The deficiency of galaxies with b/a < 0.3 is due in large part to the seeing bias noted in the previous paragraph. However, one would also expect the intrinsic number of axial ratios to drop at such low values because of the rareness of intrinsically thin disks. This bin is excluded from our analysis below.

The NUV-r color, in combination with an optical-near-IR color such as r-K, cleanly separates star-forming and quiescent galaxies, even when there are substantial amounts of dust in star-forming galaxies (Williams et al. 2009; Bundy et al. 2009). It is clear from this figure that our sample is dominated by star-forming galaxies, which is not surprising given the mass range of the sample. Galaxies in this mass range have current SFRs that are comparable to their past-averaged SFRs (i.e., the birth-parameter for these objects is ≈ 1 ; Brinchmann et al. 2004). In other words, star formation has proceeded in an approximately continuous manner over the lifetime of these galaxies. The results presented in following

sections are unchanged if we remove the few truly quiescent galaxies in our sample (galaxies with NUV-r colors greater than ≈ 4.5).

2.1. On the challenges and benefits of averaging many galaxies

In §4 we will present average colors of disk-dominated galaxies as a function of inclination. Within each bin in inclination the average colors are computed by averaging the fluxes for typically several hundred galaxies. In the absence of dust, averaging in this manner is equivalent to constructing a 'super-galaxy' that is composed of all of the stars of the galaxies in the bin. With the addition of dust attenuation, the interpretation of this averaging procedure is more complex. In this case magnitudes may be somewhat simpler to interpret because magnitudes are linear in the attenuation. Indeed, if the underlying stellar population is unchanged and only the dust content varies, then averaging magnitudes is probably the correct approach. In §4 we will present average colors computed both by averaging fluxes and averaging magnitudes in order to demonstrate that our results are insensitive to this distinction. Unless explicitly stated otherwise, our results will be computed by averaging fluxes.

The major benefit of averaging many galaxies is that the SFH of the ensemble must be smooth. As noted in the introduction, this need not necessarily be the case if one selects special classes of galaxies such as starburst or post-starburst galaxies. Our sample is composed of normal star-forming galaxies, and so our assertion that the SFH must be smooth is justified. One thus cannot appeal to sharp variations in the SFH (e.g., recent bursts) to explain the average colors of the stacked galaxies. This will prove to be an important asset when interpreting the inclination—dependent colors in §4.

3. MODELS

3.1. Stellar population synthesis

The stellar population synthesis (SPS) treatment closely follows that of Conroy et al. (2009, 2010), to which the reader is referred for details. Briefly, the code produces the evolution in time of the spectral energy distribution of a coeval set of stars from $10^{6.5}$ to $10^{10.15}$ yr, for a wide range in metallicities. Stellar evolution from the main sequence through the thermally–pulsating AGB and post–AGB phases are included. The IMF of Chabrier (2003) is adopted.

In Conroy & Gunn (2010), this SPS code was extensively calibrated against a suite of observations and was also compared to several other popular SPS codes. The version of the SPS code used herein is identical to that discussed in Conroy & Gunn (2010). We have also compared this SPS code to the predictions of the Starburst99 code (Leitherer et al. 1999; Vázquez & Leitherer 2005) for a constant SFH at solar metallicity. The spectra from these two models are very similar in the ultraviolet and optical. This agreement is encouraging because Starburst99 contains a more sophisticated treatment of massive star evolution and also includes nebular continuum emission, which is not included in our models.

The underlying stellar population in our default model will consist of solar metallicity stars that formed in a continuous, constant mode of star formation from t = 0.0 to t = 13.7 Gyr. In order to explore the impact of these assumptions we will also consider models with metallicities $Z = 0.5Z_{\odot}$ and $Z = 1.5Z_{\odot}$, and models where a fraction, c < 1, of mass forms

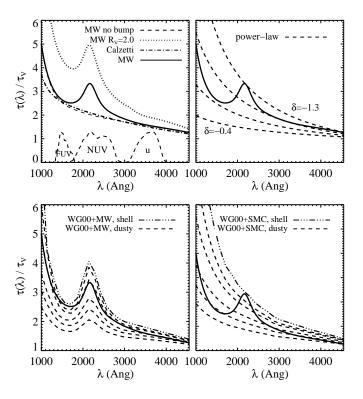


FIG. 2.— UV attenuation curves, normalized to the attenuation in the V-band. The MW curve with $R_V=3.1$ is repeated in all panels for reference. Top left: The MW curve (with $R_V=3.1$) both with and without a UV bump are compared to the Calzetti et al. attenuation curve and a MW curve with $R_V=2.0$. The transmission curves for the FUV, NUV, and u-band filters are also shown. Top right: Power-law curves of the form $\tau(\lambda) \propto \lambda^{\delta}$, with $\delta=-0.4, -0.7, -1.0$, and -1.3. Bottom panels: Attenuation curves derived from the models of WG00 for MW and SMC extinction curves are shown both for the 'shell' and 'dusty' geometries. The V-band normalized attenuation curve for the dusty geometry depends on the dust column density in the sense that larger columns yield grayer curves. In contrast, the shape of the attenuation curve for the shell geometry is independent of column density and so only one curve is seen for that geometry.

in a constant mode of star formation, the rest having formed instantly at t = 0.0. All colors considered herein have been k-corrected to the median redshift of the data, which is z = 0.04.

3.2. Dust models

A suite of phenomenological dust models are considered for the attenuation of starlight. The models are similar in spirit to the two-component dust model of Charlot & Fall (2000). This model distinguishes between attenuation suffered by young stars in their natal clouds and attenuation of all starlight due to diffuse cirrus dust.

Attenuation due to diffuse cirrus dust is described by the V-band opacity $\tau_{V,d} \equiv \tau_d$ and an attenuation curve. By 'attenuation curve' we mean the variation in attenuation optical depth with wavelength, normalized to 1.0 in the V-band, i.e., $\tau(\lambda)/\tau_V$. In this model, stars with ages younger that $t_{\rm esc}$ are subject to additional attenuation (attributed to their birth cloud) characterized by an optical depth $\tau_{V,bc} \equiv \tau_{bc}$ with an attenuation curve that in principle may differ from the curve describing the diffuse dust. Based on data from a sample of low redshift star-forming galaxies, Charlot & Fall (2000) favor values of $\tau_{bc} = 1.0$ and $t_{\rm esc} = 10^7$ yr with an attenuation

curve of the form $\tau \propto \lambda^{-0.7}$ for both components. Herein we will consider additional attenuation curves and model parameters, although for our default model we will adopt $\tau_{bc} = 0.5$ and $t_{\rm esc} = 10^7$ yr.

This two component model has strong observational motivation not only from direct observations of young stars embedded in molecular clouds but also from integrated spectra of star–forming galaxies, where the opacity measured in balmer emission lines is a factor of roughly two larger than the opacity measured from the stellar continuum (Calzetti et al. 1994).

We will also briefly consider a dust model that, in addition to the two component model described above, allows for a 'skin' of completely unobscured starlight, quantified as the fraction, f, of the stellar mass that is unobscured. Motivation for such a model comes from recent observations of extended UV emission in the outer edges of many disk galaxies (Thilker et al. 2007). The young stars in these outer regions are apparently metal–poor ($Z \sim Z_{\odot}/10$), and the extinction they suffer is small, though non-zero (Gil de Paz et al. 2007; Werk et al. 2010). In addition, it is well-known that the dust-to-gas ratio decreases with radius in disk galaxies (e.g., Issa et al. 1990; Boissier et al. 2004; Muñoz-Mateos et al. 2009), and so the outer regions of galaxies should suffer substantially less extinction than the inner regions. Finally, a sizeable fraction ($\approx 10-30\%$) of OB stars are 'runaways' that have escaped their birth clouds (Stone 1991). These stars will likely still suffer attenuation from the diffuse dust component, but nonetheless they may constitute another skin-like population that contributes a bluer than average spectrum to the integrated light.

3.2.1. Attenuation curves

We now summarize the various attenuation curves that are considered herein. Simple power-law curves are considered, characterized by an index δ such that $\tau \propto \lambda^{\delta}$. We also consider attenuation curves whose functional form is equivalent to the average extinction curve in the MW (Cardelli et al. 1989). As mentioned in the Introduction, attenuation and extinction are different concepts, but in simple geometries they can be roughly equivalent (modulo wavelength dependence of the dust albedo). When considering the MW curves we allow for the freedom to vary the strength of the UV bump, parameterized by B. In the Appendix we provide formulae for constructing MW-like extinction curves with arbitrary UV bump strength. The default MW curve is recovered for B = 1.0; for B = 0.0 there is no bump. Below we will consider an attenuation curve that resembles the MW with B = 1.0, B = 0.8, and B = 0.0. We also allow for the freedom to vary the standard extinction parameter $R_V \equiv A_V/E(B-V)$. Note that a smaller R_V corresponds to a steep extinction curve. The average extinction curve in the MW is well-fit with $R_V = 3.1$, while a value of $R_V \approx 2$ provides a good fit to the average SMC extinction curve at $\lambda \lesssim 5000 \text{Å}$ (Pei 1992). Below, when we refer to 'MW extinction' generically, we mean the standard, average MW curve with $R_V = 3.1$ and B = 1.0.

Attenuation curves produced by the models of Witt & Gordon (2000, WG00) will also be considered. These authors generate attenuation curves from both MW (adopting $R_V = 3.1$) and SMC extinction curves, taking into account the effects of scattering and geometry via radiative transfer calculations. They produce curves for three

large–scale star–dust geometries: a 'shell' geometry where all of the dust is in front of the stars (i.e., a uniform screen), a 'dusty' geometry where the stars and dust are equally mixed within a sphere, and a 'cloudy' geometry where stars and dust are equally mixed within the inner 70% of the system, with the remaining outer portion containing stars but no dust. The WG00 models assume spherical symmetry. For each of these large–scale geometries WG00 consider both a homogeneous and clumpy distribution for the local distribution of dust. There are twelve models in all (two extinction curves, three large–scale geometries, and two local geometries). Each model is computed for a wide range in column densities.

The attenuation curves considered herein are shown in Figure 2. For the WG00 models, only the homogeneous local geometries are shown, and only for the shell and dusty largescale geometries. Notice that the WG00 model constructed with a MW extinction curve and a shell geometry produces a UV bump that is stronger than is observed in the MW extinction curve. This follows from the observationally-motivated assumption that the UV bump is a true absorption feature. In contrast, the dusty geometry produces bump strengths both stronger and weaker than the bump in the MW extinction curve, depending on the overall opacity. This serves to highlight the fact that UV bumps can be either stronger or weaker than the underlying extinction curve depending on the largescale star-dust geometry. Notice also that the dusty geometries produce attenuation curves that are functions of the total dust column density in the sense that higher column densities produce grayer V-band normalized attenuation curves.

In this work we will consider the variation in broadband colors of galaxies as a function of inclination. Based on our understanding of disk-dominated galaxies, we expect the parameter τ_d , which characterizes the V-band opacity of the diffuse dust, to vary with inclination. The attenuation curve may also vary with inclination, because the dust column density will vary with inclination (e.g., Városi & Dwek 1999; Witt & Gordon 2000; Tuffs et al. 2004). However, we do not expect the dust attenuation suffered by young stars to depend on inclination, as this is a local phenomenon. We will therefore not allow the parameter τ_{bc} to vary with galaxy inclination. For our main results we will also fix the attenuation curve for the young component to be a power–law with index $\delta = -1.0$. Notice that there is no UV bump associated with the birth cloud dust.

4. RESULTS

4.1. UV colors

In Figure 3 we compare the average UV colors of a sample of disk-dominated galaxies as a function of inclination to a suite of models. Recall that the data sample consists of galaxies at 0.01 < z < 0.05 with Sersic index n < 2.5 and stellar masses in the range $9.5 < \log(M/M_{\odot}) < 10.0$. Data are binned in inclination with width 0.1, starting at b/a = 0.3. Within each bin the average flux in each filter is computed. The resulting colors redden monotonically with increasing inclination. Due to the large sample size, the errors on the mean colors are in all cases smaller than the symbol sizes. We have computed errors both via bootstrap re-sampling and the naive variance and find comparable results.

The model predictions all have the same underlying stellar population, which consists of stars with solar metallicity having formed in a constant mode of star formation from t = 0.0 to t = 13.7 Gyr. For each model starlight is attenuated ac-

⁵ Later, when we refer to 'MW attenuation' we mean an attenuation curve that is equivalent to the observed, average MW extinction curve.

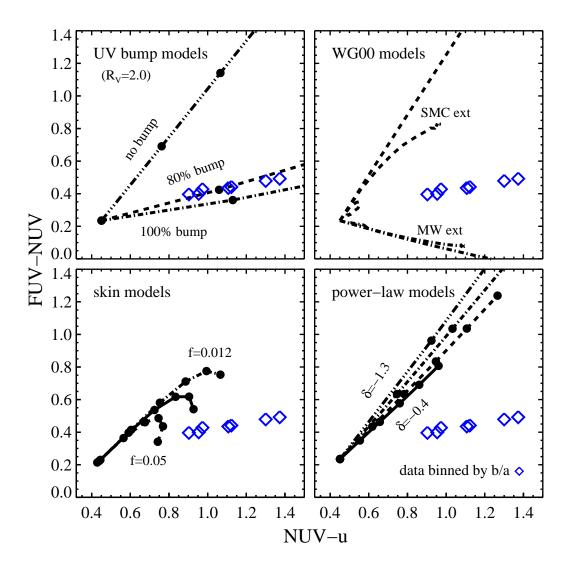


FIG. 3.— UV color–color diagrams comparing stellar population models to the average colors of low redshift disk–dominated galaxies as a function of inclination. The data points become monotonically redder in NUV–u with decreasing b/a (increasing inclination). All models assume a constant SFH, are at solar metallicity, and adopt the same attenuation prescription for young stars. The models differ only in the adopted dust attenuation curve for the diffuse dust. For each attenuation curve except for those from WG00, the trajectory in color–color space is due to an increase in the diffuse dust opacity, τ_d , from 0.0 to 1.5. The opacity increases by intervals of 0.3, as indicated by the symbols along the models. Top left: Milky Way attenuation curves with $R_V = 2.0$ and with different treatments of the UV bump at 2175Å: standard MW bump strength, no bump, 80% relative bump strength. Top right: Attenuation curves based on the WG00 dust models. Models are constructed with both SMC (dashed lines) and MW (dot-dashed lines) extinction curves. With each extinction curve, attenuation curves were derived for three dust geometries (cloudy, dusty, and shell; see text). Bottom left: Models constructed with a power-law attenuation curve ($\tau \propto \lambda^{-0.7}$), with a fraction of starlight that is completely unobscured. Fractions of f = 0.012, f = 0.025, and f = 0.050 are shown. Bottom right: Power-law attenuation curves ranging from $\lambda^{-0.4}$ to $\lambda^{-1.3}$ in steps of 0.3.

cording to a two-component dust model, the details of which are described in §3.2. The models differ principally in the attenuation curve associated with the diffuse cirrus dust. For each model, the sequence in colors is a sequence in increasing V-band optical depth, τ_d , associated with this diffuse component. The sequence increases from $\tau_d = 0.0$ to $\tau_d = 1.5$.

In the upper left panel of Figure 3 we compare the sample of disk–dominated galaxies to MW attenuation curves with $R_V = 2.0$. The curves differ only in the treatment of the UV bump at 2175Å. We consider curves with a UV bump characteristic of the average MW extinction (Cardelli et al. 1989), no UV bump, and a UV bump with strength equal to 80% of the full value (B = 0.8 in the notation of §3.2.1). A model with a UV bump strength equal to 80% of the full value pro-

vides an excellent fit to the data, while a model without a UV bump provides a poor match. For this model, the observations are reproduced for $0.2 \lesssim \tau_d \lesssim 0.5$. This range in τ_d is consistent with detailed radiative transfer models that consider inclination-dependent attenuation (Tuffs et al. 2004).

While not shown, use of the Calzetti et al. attenuation curve for starbursts produces results qualitatively similar to the no bump curve, and therefore fails to reproduce the observed trends. Also not shown are models constructed with a MW curve with $R_V = 3.1$ (the average MW value). These models also provide a poor match to the data, both for no UV bump and a bump with full strength (B = 1.0). A model with $R_V = 3.1$ and B = 0.6 provides a good fit to the UV data, although the best-fit τ_d values as inferred from the UV colors

cannot reproduce the observed optical colors (see §4.2). For this reason, the $R_V = 3.1$ model is discarded. In contrast, the inclination-dependent UV and optical colors can be well-fit with the same τ_d values for both the UV and optical colors.

We show model predictions for the attenuation curves of WG00 in the upper right panel of Figure 3. WG00 model predictions are presented for the 'homogeneous' local dust distribution, for all three large-scale geometrical configurations ('cloudy', 'dusty', and 'shell') utilizing both the MW and SMC extinction curves. For these models, unlike the others, the predictions are shown for optical depths ranging from 0.0 to 50.0. The WG00 models with MW extinction all predict FUV-NUV colors too blue compared to the data. With SMC extinction the WG00 models qualitatively resemble the models with the MW extinction curve without a UV bump shown in the upper left panel. The 'dusty' geometric configuration with SMC extinction is the model that begins to bend toward redder NUV-u colors. For this geometry the colors saturate because the attenuation curve becomes increasing greyer at high opacity (see Figure 2). One therefore cannot appeal to ever higher opacities to produce colors in better agreement with the data. The 'clumpy' local dust distribution predictions do not produce better fits to the data. It is of course possible that a different geometrical configuration not considered by WG00 may yield better agreement with the data when the SMC extinction curve is used. Also, the spherical symmetry assumed in the WG00 models may be an important limitation for our purposes. It is however beyond the scope of this paper to consider such variations to the WG00 model.

In the lower right panel we show results for power–law attenuation curves with an index that varies from $\delta = -0.4$ to $\delta = -1.3$. These models all predict FUV-NUV colors far too red at a given NUV–u color.

In the lower left panel we show results for a model constructed that is identical to the power-law attenuation model with $\delta = -0.7$ except that a skin of completely unobscured stars is added with mass fraction of f = 1-5%. This model does somewhat better at describing the data than the pure power-law models in that the dependence of the FUV-NUV color on the NUV-u color becomes shallow at large optical depths. The qualitative trends are a decent match to the data, but the quantitative predictions are much too blue in NUV-u. We will come back to this point below. Note also that the turnover in the model predictions at high opacities is generic to skin models. As the opacity increases, eventually the bulk population becomes heavily obscured and the (very blue) colors of the unobscured population dominates the integrated color. If the opacity were increased beyond what is shown in the figure, the colors would eventually approach the $\tau_d = 0.0$ colors.

It is clear from Figure 3 that none of the commonly used attenuation curves provide a good description of the observed trends with inclination. This is so because the disk-dominated sample has FUV-NUV colors that vary only slightly with inclination, while at the same time NUV-u varies by ≈ 0.5 mag. The implication is that the net attenuation in the FUV and NUV bands is comparable, i.e., $A_{\rm FUV} \approx A_{\rm NUV}$, and they both increase with increasing inclination. Most standard attenuation curves (e.g., a power-law, the form advocated by Calzetti et al. for starburst galaxies, a MW curve without a UV bump, and an SMC-based curve) do not satisfy this requirement. It is also difficult for geometrical effects to produce such a trend. The observed trend is however readily explained if the attenuation curve contains a UV bump with strength equal to 80%

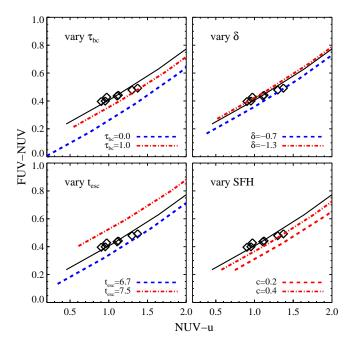


FIG. 4.— UV color–color diagram demonstrating the impact of various model assumptions. The default model ($solid\ line$), which assumes MW attenuation with a UV bump (B=0.8) and $R_V=2.0$ and a constant SFH, and the observational results (symbols), are repeated in all panels. Top left: Variation in the V–band optical depth, τ_{bc} associated with young stars. Top right: Variation in the index, δ , of the attenuation curve for the young stars. Bottom left: Variation in the time during which young stars experience additional attenuation. This time is shown in the legend in units of $\log(t/yr)$. Bottom right: Variation in the SFH. Models are shown where a smaller fraction of mass is formed in a constant mode of SFH (c=0.4 and c=0.2); the remaining mass is assumed to have formed instantly at t=0.0. Notice the different axis scales compared to Figure 3.

of the canonical MW value, and with $R_V = 2.0$. In this case the net attenuation in the FUV and NUV bands is comparable, as evidenced by the top left panel of Figure 3.

4.1.1. Assessing model assumptions

In this section we consider the consequences of model variations beyond the attenuation curve for diffuse dust. In Figure 4 we explore the impact of several important model assumptions on the UV colors. The default model here adopts the same underlying stellar population as before (constant SFH, solar metallicity), along with a MW attenuation curve with $R_V = 2.0$ and B = 0.8, $\tau_{bc} = 0.5$, a power–law attenuation with $\delta = -1.0$ for the young stars, and a transition time between young and old stars of $t = 10^7$ yr. Variations to this default model that are shown in Figure 4 include the following: no additional attenuation around young stars ($\tau_{bc} = 0.0$), twice the attenuation around young stars ($\tau_{bc} = 1.0$), an attenuation curve for young stars with an index of -0.7 and -1.3, a transition time between young and old stars, $\log(t_{\rm esc}/{\rm yr})$, of 6.7 and 7.5, and SFHs in which only a fraction of stars are formed in a constant mode of star formation (c = 0.4 and c = 0.2), the rest having formed instantly at t = 0.0.

In all cases the modifications simply result in a shift in the model locus in the FUV-NUV vs. NUV-u plane. Therefore, varying these model parameters allows us the freedom to move the model predictions in Figure 3 horizontally and/or vertically by a few tenths of a magnitude. Such shifts do not change our conclusions because the attenuation models that

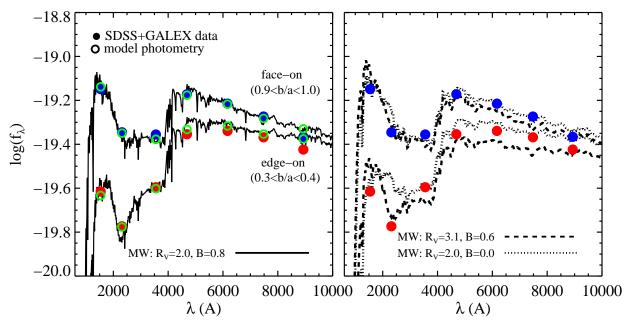


FIG. 5.— Average SEDs of face-on and edge-on star-forming galaxies with $9.5 < \log(M/M_{\odot}) < 10.0$ (solid symbols). Errors on the average SEDs are smaller than the symbol sizes. These data are compared to models with a constant SFH, $Z = Z_{\odot}$, and a MW-like attenuation curve. Left panel: Our best-fit model attenuation curve with $R_V = 2.0$ and B = 0.8. The open symbols indicate the corresponding model magnitudes computed from the model spectra. Right panel: Model attenuation curves with $R_V = 2.0$, B = 0.8 and $R_V = 3.1$, B = 0.6.

fail do so in their dependence of FUV-NUV on NUV-u. In other words, allowing the freedom to shift the models arbitrarily does not produce significantly better fits to the data, except for the skin models and the B=1.0 UV bump model; see below. Modifying the 'zero-point' of the models will however clearly change the quantitative conclusions drawn from this figure, such as the average SFH and total dust opacity, but that is to be expected when only considering UV colors.

The only cases where a shift in the NUV–u color may result in a better model fit is for the skin models and the B=1.0 bump model. For the skin model, moving the model NUV–u colors redward by ≈ 0.4 mag would yield an improved agreement between the skin models and the data. Such a shift can be induced by a SFH where only 20% of the mass forms in a constant mode (c=0.2), the rest having formed instantly at t=0.0. Below we show that such SFHs can be ruled out by the optical colors of our disk–dominated sample. For the B=1.0 bump model, a shift redward in FUV-NUV of ≈ 0.1 mag, induced for example by choosing $t_{\rm esc}=10^{7.5}$ yr, would yield a good match with the data. We leave this as an open possibility, noting that such a shift would only strengthen our conclusion that a strong 2175Å absorption feature was required to match the observations.

4.2. Constraints from optical colors

We now turn to optical colors in order to gain additional insight into the dust and stellar population content of our sample. In Figure 5 we show the average spectral energy distributions (SEDs) for galaxies in our highest and lowest inclination bins. SEDs were constructed from *GALEX* and SDSS photometry. We also include in this figure our favored model, which has a constant SFH, $Z = Z_{\odot}$, and a MW dust attenuation curve with $R_V = 2.0$ and B = 0.8 (models with $R_V = 2.0$, B = 0.0 and $R_V = 3.1$, B = 0.6 are also shown for comparison). The models for the face-on and edge-on galaxies differ only in the V-band optical depth associated with diffuse dust, τ_d .

Clearly our favored model matches the data well over the interval $1500\text{\AA} \lesssim \lambda \lesssim 9000\text{Å}$, providing further support for the assumptions made in our favored model. The strong depression in the SED of edge-on galaxies at $\lambda \approx 2200\text{Å}$ is striking, and strongly suggestive of the presence of the UV bump.

The disagreement between the models and data in the z-band is noteworthy. Unfortunately, no significant conclusions can be drawn from this disagreement because the SED of star-forming galaxies at $\lambda \gtrsim 7000 \text{Å}$ is sensitive to the presence of thermally-pulsating asymptotic giant branch stars (e.g., Maraston 2005). The modeling of this stellar evolutionary phase is very uncertain (e.g., Conroy et al. 2009, 2010), and minor modifications to the bolometric luminosity and temperature of these stars can readily account for the disagreement seen in the figure.

In order to further assess our model assumptions, in Figure 6 we consider optical color–color plots. In this figure the SDSS photometry is compared to models that differ in their attenuation curve associated with diffuse dust (left panel), and models that differ in their assumed SFH. Note that the model *ugriz* photometry is insensitive to the presence of a UV bump, and so we do not distinguish between MW attenuation with or without a UV bump in this figure.

The variations in SFH result in significant differences in these ugr color-color plots. Notice that the bluest points in both the c=0.4 and c=0.2 SFH models are redder than the bluest data points. This implies that these SFHs cannot possibly fit our disk-dominated sample (recall that a single SFH must be able to fit the colors for all inclination bins, since SFH will not vary with inclination). As mentioned in §2, this is not surprising in light of results from detailed modeling of the spectra of galaxies with masses comparable to those considered herein (e.g., Salim et al. 2007; Brinchmann et al. 2004). We note in passing that the SFH models considered herein produce UV and optical colors that are almost indistinguishable from τ -model SFHs with $\tau=5$ and 8 Gyr corresponding

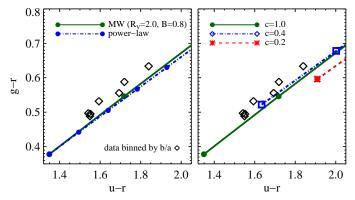


FIG. 6.— Optical color–color plots as a function of inclination compared to various models. Left panel: Comparison of MW (with $R_V = 2.0$ and B = 0.8) and power-law (with $\delta = -0.7$) attenuation curves. Here the SFH is constant (c = 1.0). Each model is a sequence in optical depth associated with diffuse dust, in steps of $\Delta(\tau_d) = 0.3$. Right panel: Models with the same MW attenuation curve but varying SFH. The SFHs are varied such that a fraction, c, of the mass is formed in a continuous mode of star formation, with the rest having formed instantly at z = 0.0.

to c = 0.2 and c = 0.4.

As discussed in $\S4.1.1$, the skin model shown in the lower left panel of Figure 3 could be brought into agreement with the data if a SFH with c=0.2 were adopted. While not shown, the optical colors for the skin model are identical to those in Figure 6 for the MW curve because the flux contributed by the skin is negligible in the optical. The results from this figure therefore allow us to confidently rule out the skin models because the SFH necessary to reconcile the model with the UV colors grossly fails to match the optical colors.

As mentioned in 4.1, a model with $R_V = 3.1$ and B = 0.6 also provided a good fit to the UV colors. However, as shown in Figure 5, this model cannot simultaneously match the entire UV through near-IR SEDs of star-forming galaxies. The disagreement is particularly striking for the NUV-u colors, where the constraints on low values for R_V are strongest.

4.3. Trends with stellar mass and metallicity, and variation in data analysis

We now return to the UV colors. In Figure 7 we explore the sensitivity of the results shown in Figure 3 to the sample selection and method of data analysis. In this figure we consider galaxies both more and less massive than our fiducial sample, and galaxies split according to their gas—phase metallicity. In the latter case we consider a wider bin in mass, $9.0 < \log(M/M_{\odot}) < 10.0$, in order to increase statistics. In the panel showing the dependence on metallicity, we also show the change in model colors accompanying a change in metallicity of the underlying stellar population from $0.4Z_{\odot}$ to Z_{\odot} . Model predictions for the default set of assumptions are included in this figure, where we have adopted a MW attenuation curve with $R_V = 2.0$ and with UV bump strengths B = 0.0, 0.8, 1.0. These model predictions are identical to those shown in the upper left panel of Figure 3.

The observed trends are generally as expected: more massive and more metal-rich galaxies are redder in both NUV-u and FUV-NUV, although the differences are not large. There is tentative evidence that the more massive galaxies deviate from our favored model in the sense that their FUV-NUV colors are ≈ 0.1 mag bluer than expected for edge-on galaxies. While we are hesitant to interpret this trend, if real it could

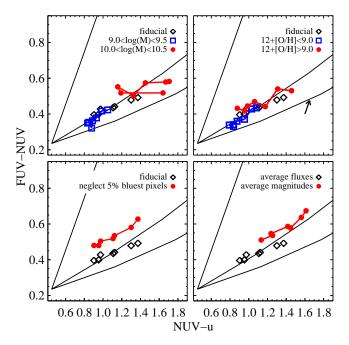


FIG. 7.— Color–color diagram comparing a variety of different selection criteria and methods of data analysis. Models with a MW attenuation curve with varying UV bump strength (B=0.0,0.8,1.0) are included for comparison (solid lines; these models are identical to the models shown in the upper left panel of Figure 3). In each panel the fiducial sample is shown as diamonds. Notice the different axis scales compared to Figure 3. Upper left: Samples selected with stellar masses $9.0 < \log(M/M_{\odot}) < 9.5$ and $10.0 < \log(M/M_{\odot}) < 10.5$. Upper right: Samples selected with 12+[O/H] < 9.0 and 12+[O/H] > 9.0 drawn from a parent sample with $9.0 < \log(M/M_{\odot}) < 10.0$. The arrow indicates the change in colors accompanying a change in Z of the underlying stellar population from $0.4Z_{\odot}$ to Z_{\odot} . Lower left: FUV-NUV color computed after removing the 5% bluest pixels. Lower right: Comparison between colors of the fiducial sample computed by averaging magnitudes and averaging fluxes.

indicate a stronger UV bump in more massive galaxies.

The observed weak dependence on metallicity is generally consistent with being due to the underlying stellar population, under the assumption that variation in gas-phase metallicity is accompanied by a similar change in the stellar metallicity.

In Figure 7 we also show the observed trend where we have computed the FUV-NUV color after masking the bluest 5% of pixels. This masking was done to test the extent to which the observed trend (namely, the weak trend of FUV-NUV vs. inclination) is due to a few very blue and concentrated regions of star formation. The NUV-u color was not re-computed with this masking because of the complications in translating the masks in the GALEX pixels into the SDSS pixels. The resulting FUV-NUV colors are on average ≈ 0.1 mag redder than the colors computed from all of the pixels. The results from this exercise demonstrate that the observed very blue FUV-NUV colors even for the most inclined galaxies cannot be attributed to a few very blue concentrated star–forming regions.

Finally, in this same figure we show how the average colors of our fiducial sample depends on the method of averaging. We show average colors computed by averaging fluxes (our standard approach) and by averaging magnitudes. As mentioned in §2.1, in the absence of dust, averaging fluxes is the correct approach. In the presence of dust, there is no clearly preferred method, although we note that the attenuation by dust is averaged in a more meaningful way when averaging

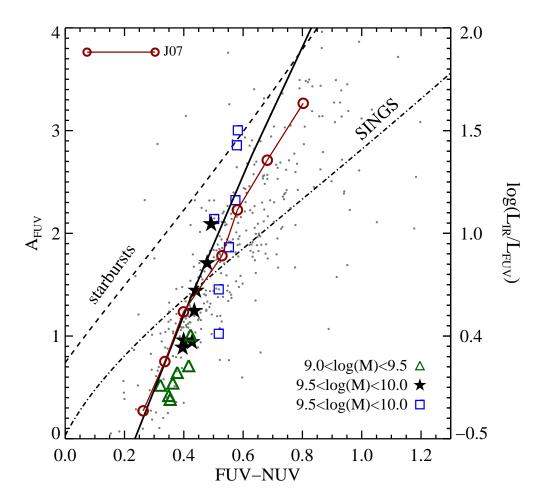


FIG. 8.— Total FUV attenuation as a function of FUV-NUV color (analog of the IRX- β relation). Lines show the relation for starburst galaxies (*dashed line*; Kong et al. 2004), for galaxies in the SINGS survey (*dot-dashed line*; Muñoz-Mateos et al. 2009), and our best-fit model that contains a strong UV bump (*solid line*). For the starburst and SINGS samples, $A_{\rm FUV}$ is estimated from $L_{\rm IR}/L_{\rm FUV}$ according to the relation provided by Buat et al. (2005). For our samples of disk-dominated galaxies (*diamond, star, and square symbols*), $A_{\rm FUV}$ is estimated as described in the text. We show results for three bins in stellar mass, as indicated in the legend. Small symbols are from the work of Johnson et al. (2007a, J07); larger connected symbols are median FUV-NUV colors from J07 computed in bins of $A_{\rm FUV}$.

magnitudes. Regardless, the resulting average inclination-dependent colors are largely unaffected by our choice of averaging.

4.4. The IRX- β relation

Recall that the IRX- β relation compares the UV spectral slope, β , to the ratio of total infrared to UV luminosity, the latter being a fairly direct probe of the total UV attenuation. In theory, an IRX- β relation therefore provides a simple estimate of the net attenuation in the UV based solely on the UV slope (i.e., the FUV-NUV color). In practice, this procedure is complicated not only by the large observed scatter in the relation, but also by the fact that starburst and 'normal' star-forming galaxies follow different relations (Meurer et al. 1999; Dale et al. 2007; Boissier et al. 2007), and the fact that the relation depends on SFH (Kong et al. 2004; Cortese et al. 2008).

In Figure 8 we translate our results into an analog of the IRX- β relation. Specifically, we estimate the attenuation in the FUV, $A_{\rm FUV}$, of the observed galaxies from their g-r color by simply comparing the model colors to the observed colors in order to estimate the total net attenuation [i.e., $A_{\rm FUV} \propto$

 $\ln(F_i^{\rm FUV}/F_o^{\rm FUV})$ where i and o denote the dust–free and dust reddened model spectra, respectively]. We obtain similar results when using other colors to estimate $A_{\rm FUV}$. We then shift our estimated $A_{\rm FUV}$ values down by 0.8 mag in order to match the locus of previous results (see below). The particular values of $A_{\rm FUV}$ will clearly depend on our model assumptions (e.g., the assumed SFH), but the general behavior of our results in the IRX- β should be robust. Results are shown for three stellar mass bins.

In this figure we include the IRX $-\beta$ relation estimated for a sample of local starburst galaxies (Meurer et al. 1999; Kong et al. 2004), and normal star–forming galaxies from the SINGS survey (Muñoz-Mateos et al. 2009). The 'IRX' portion of these relations has been converted into A_{FUV} via the formula provided in Buat et al. (2005).

The most striking conclusion to be drawn from Figure 8 is that our sample spans a large range in $A_{\rm FUV}$ but a comparatively narrow range in FUV-NUV color, i.e., our results imply an extremely steep IRX- β relation. The relation for our sample of disk-dominated galaxies is much steeper than either the starburst or normal star-forming galaxy relation. This result is driven entirely by the fact that while FUV-NUV varies

little in our sample, other colors, such as NUV-u, u-r, and g-r vary significantly. The trend for the highest stellar mass bin is notable in that it appears to be steeper than our favored model. As mentioned in §4.3, if real this trend could point to a stronger UV bump in more massive galaxies.

The IRX $-\beta$ relation from the SINGS sample is representative of the entire SINGS sample, excluding only three starburst galaxies and galaxies with FUV-NUV>0.9 (Muñoz-Mateos et al. 2009). It is therefore not surprising that the SINGS relation is much shallower than ours, because their sample contains galaxies with a wide range in SFHs. Indeed, from Figure 3 in Muñoz-Mateos et al. (2009) it is apparent that their IRX $-\beta$ relation is driven largely by variations in SFH, in the sense that galaxies with redder FUV-NUV colors have formed the bulk of their stars at earlier epochs. In contrast, the IRX $-\beta$ relation derived herein is characteristic of a single SFH (for each stellar mass bin), and therefore our relation is truly a sequence in dust opacity.

In this figure we also compare our results to Johnson et al. (2007a, J07) who computed the IRX- β relation for \approx 1000 galaxies using observations from GALEX and $Spitzer^6$. We show their results for all galaxies with $D_n4000 < 1.5$, where D_n4000 is a measure of the strength of the 4000Å break. D_n4000 is a measure of the age of the stellar population that is relatively insensitive to dust. This cut on D_n4000 selects actively star-forming galaxies, similar to those in our own sample. For this sample we also show the median FUV-NUV color in bins of $A_{\rm FUV}$, where the FUV attenuation has been estimated from IRX using the formula in Buat et al. (2005).

The average relation from J07 is in excellent agreement with our observational results and also with our favored model that includes a strong UV bump in the diffuse dust attenuation curve, after we shift our results downward in Figure 8 by 0.8 mag. We stress that the solid line in Figure 8 is *not* a fit to the average relation from J07. Rather, the agreement is remarkable independent confirmation of our best-fit model. We will discuss the implications of this result in the following section.

The required shift of our results 0.8 mag downward to match the results from J07 deserves further comment. Note first that the results from J07 and those derived herein are not directly comparable, as J07 measure IRX while we only measure UV through near-IR SEDs. Any attempted comparison between our work and J07 will therefore be model-dependent. A detailed analysis of this issue is beyond the scope of the present article. However, irrespective of our results, notice that the implied A_{FUV} vs. FUV–NUV relation in the J07 sample extrapolates to $A_{FUV} = 0.0$ at a FUV-NUV color significantly redder than canonical dust-free solar metallicity stellar population predictions (FUV-NUV ≈ 0). This indicates that there may be some modeling error in translating IRX (which J07 actually measure) into A_{FUV} (which was derived from IRX via the relation from Buat et al. 2005), at least at low attenuation.

5. DISCUSSION

5.1. An emerging physical picture, and implications

In the previous section we demonstrated that the inclination-dependent UV colors of a mass-selected sample of disk-dominated galaxies are best explained by a MW at-

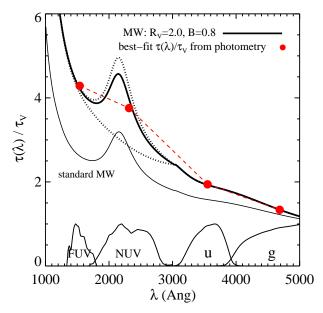


FIG. 9.— Attenuation curves normalized to the V-band. The dotted curves show MW attenuation curves with $R_V = 2.0$, both for a standard UV bump strength and no UV bump (B = 1.0 and B = 0.0, respectively). The thick solid line is our best-fit attenuation curve with $R_V = 2.0$ and a UV bump strength equal to 80% of the standard MW value. The thin solid line is the standard MW curve (i.e., with $R_V = 3.1$ and B = 1.0). The points show the actual constraints on the attenuation curve provided by the broadband photometry. Transmission curves with arbitrary normalization are included for the FUV, NUV, u, and g filters.

tenuation curve with $R_V = 2.0$ that includes a prominent UV bump at 2175Å. The strength of this bump is approximately 80% as strong as the average UV bump observed in the MW. This result is summarized in Figure 9. In this figure we show our favored attenuation curve and compare this to the standard MW curve ($R_V = 3.1$). We also show the actual constraints on the attenuation provided by the FUV, NUV, u, and g filters. It is clear from this figure that while our results are consistent with a strong UV bump, we cannot claim that our results require a UV bump, since we rely solely on broadband photometry over a narrow redshift range. However, inspection of Figure 5 strongly suggests that the UV bump is responsible, as we know of no other model variation capable of reproducing the depression in the average SED of edge-on galaxies at $\lambda \approx 2200\text{Å}$.

Our results imply that previous work attempting to measure the SFR in low redshift galaxies has underestimated the amount of attenuation in the near-UV. From inspection of Figure 9 we can see that typical attenuation in the NUV band is underestimated by approximately the value of the V-band optical depth, τ_V , when comparing standard attenuation curves (power-law, starburst, and average MW) to our favored model. For moderately dusty galaxies the underestimation may therefore be substantial. The bias is such that SFRs based primarily on the near-UV will be lower than the intrinsic SFR. Additional work will be required to understand in detail how the effects of a strong UV bump propagate into the derived physical properties of galaxies.

From this figure we can also understand qualitatively why our disk-dominated sample favors an attenuation curve with $R_V = 2.0$, as opposed to the canonical value of $R_V = 3.1$ pre-

⁶ The data from J07 shown in Figure 8 are revised quantities based on the same sample as in J07. The most significant change with respect to the data presented in J07 is the use of updated *GALEX* photometry, which results in bluer FUV-NUV colors by ≈ 0.05 − 0.1 mag.

ferred in the MW.⁷ Decreasing R_V from 3.1 to 2.0 results in substantially more attenuation between the u and NUV filters, and therefore a much redder NUV–u color. The relative attenuation between FUV and NUV, and also between u and g is does not change substantially between the $R_V = 3.1$ and $R_V = 2.0$ curves, and so these colors change by much less than NUV–u. Therefore, it is principally the constraint from the NUV–u color that drives the requirement for $R_V \approx 2.0$.

If our interpretation of the observed trends is correct, this would constitute the first detection of the UV bump in the attenuation properties of galaxies at low redshift. The only other detection of the UV bump in the attenuation curves of galaxies was reported by Noll et al. (2009), who considered restframe UV spectra of star-forming galaxies at $z \sim 2$. In Conroy (2010) the observed B-R colors of star-forming galaxies at 0.7 < z < 1.4 were used to constrain the average strength of the UV bump. A bump as strong as observed in the MW was ruled out for $R_V = 3.1$, as we find herein, but a UV bump strength needed to match our sample ($B \approx 0.8$ with $R_V = 2.0$, which, in the UV, is comparable to $B \approx 0.6$ with $R_V = 3.1$) could not be ruled out. More detailed modeling of the $z \sim 1$ population will be required to place stronger constraints on the presence of the UV bump. Luckily, the necessary data already exists.

It is important to understand why evidence of the UV bump in the attenuation curve of galaxies has proved elusive until now. Many authors have previously attempted to model the UV colors of galaxies with a standard MW attenuation curve (i.e., with $R_V = 3.1$ and B = 1.0). In all cases the MW curve was found to be a poor fit, as we find herein. The reduction in the strength of the UV bump to B = 0.8, accompanied by our choice of $R_V = 2.0$, is essential for our attenuation models to fit the data. Recall again that an attenuation curve with $R_V = 2.0$ and B = 0.8 yields FUV-NUV colors comparable to an attenuation curve with $R_V = 3.1$ and B = 0.6. In other words, if considering only the UV and $R_V = 3.1$ MW-like attenuation curves, a significant depression of the UV bump is required. Clearly, ruling out the standard MW curve does not imply that observed galaxies show no evidence for a UV bump. In addition, considering the UV colors of galaxies as a function of inclination allowed us to confidently separate stellar population effects from dust attenuation effects.

These results must somehow be reconciled with the wellknown fact that local starburst galaxies show no evidence for a UV bump (e.g., Calzetti et al. 1994). It has been conjectured that either metallicity, intensity of the interstellar radiation field, or the star-dust geometry modulates the strength of the UV bump. The dust model of Silva et al. (1998), as explored in Granato et al. (2000), provides a plausible path toward reconciling our results with those for the starburst galaxies. Granato et al. showed that an underlying MW extinction curve (applied to dust in the diffuse ISM) can give rise to a starburst attenuation curve similar to that observed by Calzetti et al., and can also give rise to an attenuation curve with a significant UV bump for 'normal' star-forming galaxies. In their model the difference is due to geometry: for the starbursts the UV dust attenuation is dominated by dust within the molecular clouds in which the young stars are embedded, because the fraction of young stars is high in starbursts. The molecular clouds are optically thick, and so the resulting attenuation curve is governed primarily by the wavelength-dependent fraction of the intrinsic flux emitted by young stars. In the case of normal star-forming galaxies, a significant fraction of UV photons are emitted by stars that have left their birth clouds, and so the only attenuation they suffer is due to the optically thin diffuse ISM, which may imprint a UV bump.

More recently, (Panuzzo et al. 2007) have used the Silva et al. dust models to interpret the IRX- β relation for normal SF galaxies and conclude that the data are consistent with a UV bump in the extinction curve. These authors highlight the important role of age-dependent extinction on the resulting attenuation curve. Inoue et al. (2006) consider the effects of dust scattering in detail and conclude that the data are consistent with a UV bump. Finally, Burgarella et al. (2005) take an empirical approach in modeling UV attenuation similar to what we do herein, and conclude that the observed IRX- β relation for normal SF galaxies is consistent with a UV bump with half the strength of the UV bump in the MW extinction curve. All of these studies provide additional support to our principle conclusion regarding the presence of a UV bump in the attenuation curve of normal SF galaxies.

While the Silva et al. model is capable of explaining the absence of a UV bump in starburst galaxies and its presence in normal star-forming galaxies by geometrical effects, other possibilities remain. The most plausible alternative explanation is the preferential destruction of the grains responsible for the UV bump in the harsh interstellar radiation characteristic of starburst galaxies. PAH emission in the IR is known to be modulated by the strength of the radiation field in the sense that harder radiation fields result in diminished (or even negligible) PAH emission (e.g., Voit 1992; Madden et al. 2006; Smith et al. 2007). These properties of PAHs can provide a natural explanation for the variation in UV bump strength, if PAHs are responsible for the absorption at 2175Å. More directly, the UV bump is absent in the extinction curve probed by four out of five sightlines in the SMC (Pei 1992), which may be due to the harsher radiation field there (Gordon et al. 2003). Metallicity is an unlikely explanation for the difference between starburst and normal galaxies because the gasphase metallicities of these two types of galaxies are not substantially different (Calzetti et al. 1994; Tremonti et al. 2004). Now that we have identified samples of galaxies that plausibly contain a UV bump, each of these scenarios can be tested.

In Figure 8, we showed that the average relation between total UV attenuation and UV spectral slope is extremely steep in the sense that a narrow range in observed spectral slope (i.e., FUV-NUV color) corresponds to a large range in UV attenuation. These results extend and strengthen previous results that also found very steep relations (e.g., Bell 2002; Johnson et al. 2007b). In our interpretation, the steepness of this relation is due to the properties of the average attenuation curve for a fixed average SFH. In essence, the attenuation curve flattens considerably over the wavelength range probed by the FUV and NUV filters (1500Å $\lesssim \lambda \lesssim 2300$ Å), and so large variation in the total attenuation produces little change in FUV-NUV colors. Appeal to the UV bump at 2175Å provides a natural explanation for the observed flattening in the attenuation curve. The shallower IRX $-\beta$ relations found in previous work arises from the fact that previous relations were constructed from samples of galaxies spanning a wide range of SFHs.

We have presented *average* UV colors as a function of inclination and UV attenuation. For individual galaxies, one can

Of course, as emphasized throughout, attenuation and extinction are conceptually different, and so there is no a priori reason for the attenuation curve that best describes our sample to be similar to the average extinction curve measured for the MW.

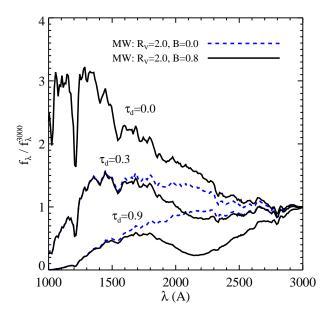


FIG. 10.— Restframe UV spectra of two models that differ only in the strength of the UV bump at 2175\AA . One model has no UV bump while the other has a UV bump with strength 80% of the average MW strength. Each model is a sequence in optical depth characterizing the diffuse dust component: $\tau_d = 0.0, 0.3, 0.9$. The spectra are normalized to the flux at 3000\AA .

expect variations about these average relations due to variations in either the star-dust geometry, SFH, metallicity, or dust-to-gas ratio. Indeed, within a given inclination bin the spread in FUV-NUV colors is large ($\sigma\approx 0.5$ mag). We speculate that variation in the SFH over the last $\sim 10^8$ yr and variation in the star-dust geometry are the two largest sources of scatter. In addition, we clearly detect systematic changes in the FUV-NUV color with stellar mass, which may either be due to a varying attenuation curve or possibly a varying average SFH with galaxy mass.

In light of the steepness of the IRX $-\beta$ relation for a given SFH as measured herein, its dependence on the SFH, and the expected galaxy-to-galaxy scatter due to variations in other physical properties, we conclude that the uncertainties in estimating UV attenuation based on the observed UV slope are very large and believe that this calls the utility of the IRX $-\beta$ relation into question. This conclusion applies when β —the UV slope—is measured over a wavelength interval including the UV bump. If this spectral range is avoided then the IRX $-\beta$ relation may yield more reliable results. Care must clearly be taken when estimating β from either spectroscopy or photometry.

5.2. Future directions

The results contained in this work present clear directions for future work. First, moderate resolution spectra in the UV would provide conclusive evidence for the UV bump. In Figure 10 we show the restframe UV spectra for our default stellar population model (constant SFH and solar metallicity), for two dust attenuation curves that differ only in the strength of the UV bump. We show models both for a bump strength of 80% (the favored dust model) and zero bump strength. Spectra are shown for three values of the V-band optical depth characterizing the diffuse dust: $\tau_d = 0.0, 0.3, 0.9$. The treatment of dust surrounding young stars is constant and the same as previous sections. For reference, the average inclination

dependent colors of our disk-dominated sample can be reproduced in our favored model for $0.2 \lesssim \tau_d \lesssim 0.5$.

This figure demonstrates that UV spectra of moderately dusty galaxies would provide a clear test of our preferred model. Our sample of highly inclined disk-dominated star-forming galaxies would be ideal for these purposes. Narrow band photometry around 2175Å could also potentially reveal the unique signature of the UV bump. The required filters are already on-board the *Hubble Space Telescope*.

If the UV bump is indeed responsible for the observed trends, the next task will be to identify whether or not PAHs are responsible for the absorption. Recall that the identity of the grain(s) responsible for the UV bump is still a mystery, and, while PAHs are a plausible candidate, other possibilities remain (including, e.g., graphite; Draine & Malhotra 1993). If PAHs are responsible, then one would expect to uncover a strong correlation between PAH emission in the infrared (traced for example by the $8\mu m$ channel on the *Spitzer Space Telescope*; Muñoz-Mateos et al. 2009) and a strong UV bump (traced for example by the FUV-NUV color).

An especially promising direction would be to consider galaxies with gas-phase metallicities both above and below 12+[O/H]= 8.1. Based on data from the SINGS survey, Draine et al. (2007) found that galaxies above this metallicity contained a wide range of PAH emission strengths, whereas below this value galaxies were deficient in PAH emission. We would therefore expect the trends of FUV-NUV with inclination to change qualitatively below this metallicity scale, again assuming that PAHs are the cause of the UV bump. According to Tremonti et al. (2004), galaxies with such low gas-phase metallicities have stellar masses $\log(M/M_{\odot}) \lesssim 8.5$. Irregular galaxies are more common than disk-dominated galaxies at this mass scale, and so it may be difficult to separate trends with geometry from trends with PAH abundance across this mass scale. Nonetheless, with detailed modeling the PAH hypothesis may be tested with the approach outlined above.

6. SUMMARY

In this work, we measure the UV and optical colors of diskdominated galaxies at 0.01 < z < 0.05 as a function of their inclination. These inclination-dependent colors provide powerful constraints on dust attenuation models because the observed trends cannot be caused by variations in the underlying stellar populations. The observed inclination-dependent FUV-NUV and NUV-u colors cannot be explained by common dust attenuation curves, including power-law models, standard MW and SMC curves, nor the attenuation curve measured for starbursts (Calzetti et al. 1994). After considering a number of model variations, we are led to conclude that the strong dust feature at 2175Å (the UV bump) seen in the MW extinction curve is responsible for the observed trends. In order to simultaneously fit the UV and optical colors, we require an attenuation curve analogous to the MW extinction curve with $R_V \equiv A_V/E(B-V) \approx 2.0$ and a UV bump strength equal to 80% of the standard MW value. Previous work failed to recognize the importance of the UV bump because only standard MW curves were considered ($R_V = 3.1$, full UV bump strength), and these consistently fail to match observed trends.

We also construct an analog of the IRX- β relation and find that the inferred relation between UV slope and FUV attenuation is extremely steep. Our derived relation agrees well with recent work that combines UV and IR photometry for ≈ 1000 low redshift galaxies (Johnson et al. 2007a), but is much steeper than the starburst relation. Our results provide

a natural interpretation of the IRX- β relations found in previous work. Namely, for a given SFH, the IRX- β relation will be very steep because of the properties of the attenuation curve. Varying the SFH will produce primarily horizontal shifts in this relation. When considering heterogeneous samples of galaxies with a range of SFHs, the IRX- β relation will on average appear shallow, due to the range in SFHs, but will show tremendous scatter, due to the attenuation curve. From the steepness of this relation for a given SFH, we conclude that it is not possible to accurately correct for dust attenuation — even in an average sense — based solely on the UV slope.

Confirmation of our interpretation must await UV spectroscopic follow-up. If confirmed, these results will pave the way toward finally identifying the grain population responsible for the 2175Å extinction feature. In addition, these results necessitate a more nuanced interpretation of the UV spectral slopes of star-forming galaxies.

CC is supported by the Porter Ogden Jacobus Fellowship at Princeton University. We thank the MPA/JHU collaboration for making their catalogs publically available, and Bruce Draine for comments on an earlier draft. We also thank Ben Johnson for providing an updated version of his data used in our Figure 8.

Funding for the Sloan Digital Sky Survey (SDSS) has been provided by the Alfred P. Sloan Foundation, the Participating Institutions, the National Aeronautics and Space Administration, the National Science Foundation, the U.S. Department of Energy, the Japanese Monbukagakusho, and the Max Planck Society. The SDSS Web site is http://www.sdss.org/.

The SDSS is managed by the Astrophysical Research Consortium (ARC) for the Participating Institutions. The Participating Institutions are The University of Chicago, Fermilab, the Institute for Advanced Study, the Japan Participation Group, The Johns Hopkins University, Los Alamos National Laboratory, the Max-Planck-Institute for Astronomy (MPIA), the Max-Planck-Institute for Astrophysics (MPA), New Mexico State University, University of Pittsburgh, Princeton University, the United States Naval Observatory, and the University of Washington.

This work made extensive use of the NASA Astrophysics Data System and of the astro-ph preprint archive at arXiv.org.

REFERENCES

Adelman-McCarthy, J. K. et al. 2008, ApJS, 175, 297 Bell, E. F. 2002, ApJ, 577, 150 Bianchi, L., Clayton, G. C., Bohlin, R. C., Hutchings, J. B., & Massey, P. 1996, ApJ, 471, 203 Blanton, M. R. & Roweis, S. 2007, AJ, 133, 734 Blanton, M. R. et al. 2005, AJ, 129, 2562 Boissier, S., Boselli, A., Buat, V., Donas, J., & Milliard, B. 2004, A&A, 424, Boissier, S. et al. 2007, ApJS, 173, 524 Bouwens, R. J., Illingworth, G. D., Franx, M., Chary, R., Meurer, G. R., Conselice, C. J., Ford, H., Giavalisco, M., & van Dokkum, P. 2009, ApJ, Brinchmann, J., Charlot, S., White, S. D. M., Tremonti, C., Kauffmann, G., Heckman, T., & Brinkmann, J. 2004, MNRAS, 351, 1151 Buat, V. et al. 2005, ApJ, 619, L51 Bundy, K. et al. 2009, ArXiv:0912.1077 Burgarella, D., Buat, V., & Iglesias-Páramo, J. 2005, MNRAS, 360, 1413 Calzetti, D. 2001, PASP, 113, 1449 Calzetti, D., Armus, L., Bohlin, R. C., Kinney, A. L., Koornneef, J., & Storchi-Bergmann, T. 2000, ApJ, 533, 682 Calzetti, D., Kinney, A. L., & Storchi-Bergmann, T. 1994, ApJ, 429, 582 Calzetti, D. et al. 2005, ApJ, 633, 871 Capak, P. et al. 2009, ArXiv:0910.0444 Cardelli, J. A., Clayton, G. C., & Mathis, J. S. 1989, ApJ, 345, 245 Chabrier, G. 2003, PASP, 115, 763 Charlot, S. & Fall, S. M. 2000, ApJ, 539, 718 Conroy, C. 2010, MNRAS, 404, 247 Conroy, C. & Gunn, J. E. 2010, ApJ, 712, 833 Conroy, C., Gunn, J. E., & White, M. 2009, ApJ, 699, 486 Conroy, C., White, M., & Gunn, J. E. 2010, ApJ, 708, 58 Cortese, L., Boselli, A., Franzetti, P., Decarli, R., Gavazzi, G., Boissier, S., & Buat, V. 2008, MNRAS, 386, 1157 da Cunha, E., Charlot, S., & Elbaz, D. 2008, MNRAS, 388, 1595 da Cunha, E., Eminian, C., Charlot, S., & Blaizot, J. 2010, MNRAS, 403,

Dale, D. A. et al. 2007, ApJ, 655, 863

Draine, B. T. 2003, ARA&A, 41, 241

Draine, B. T. et al. 2007, ApJ, 663, 866

Elbaz, D. et al. 1999, A&A, 351, L37

Elíasdóttir, Á. et al. 2009, ApJ, 697, 1725

Draine, B. T. & Malhotra, S. 1993, ApJ, 414, 632

P. D., & de Propris, R. 2007, MNRAS, 379, 1022

- 2009. ArXiv:0903.1658.

Disney, M., Davies, J., & Phillipps, S. 1989, MNRAS, 239, 939

Driver, S. P., Popescu, C. C., Tuffs, R. J., Liske, J., Graham, A. W., Allen,

Engelbracht, C. W., Gordon, K. D., Rieke, G. H., Werner, M. W., Dale, D. A., & Latter, W. B. 2005, ApJ, 628, L29 Galliano, F., Dwek, E., & Chanial, P. 2008, ApJ, 672, 214 Gil de Paz, A. et al. 2007, ApJ, 661, 115 Giovanelli, R., Haynes, M. P., Salzer, J. J., Wegner, G., da Costa, L. N., & Freudling, W. 1994, AJ, 107, 2036 -. 1995, AJ, 110, 1059 Gordon, K. D., Clayton, G. C., Misselt, K. A., Landolt, A. U., & Wolff, M. J. 2003, ApJ, 594, 279 Goudfrooij, P., Hansen, L., Jorgensen, H. E., & Norgaard-Nielsen, H. U. 1994, A&AS, 105, 341 Granato, G. L., Lacey, C. G., Silva, L., Bressan, A., Baugh, C. M., Cole, S., & Frenk, C. S. 2000, ApJ, 542, 710 Inoue, A. K., Buat, V., Burgarella, D., Panuzzo, P., Takeuchi, T. T., & Iglesias-Páramo, J. 2006, MNRAS, 370, 380 Issa, M. R., MacLaren, I., & Wolfendale, A. W. 1990, A&A, 236, 237 Jarrett, T. H., Chester, T., Cutri, R., Schneider, S., Skrutskie, M., & Huchra, J. P. 2000, AJ, 119, 2498 Johnson, B. D. et al. 2007a, ApJS, 173, 377 . 2007b, ApJS, 173, 392 Kauffmann, G. et al. 2003, MNRAS, 341, 33 Knapp, G. R., Guhathakurta, P., Kim, D., & Jura, M. A. 1989, ApJS, 70, 329 Kong, X., Charlot, S., Brinchmann, J., & Fall, S. M. 2004, MNRAS, 349, 769 Leger, A. & Puget, J. L. 1984, A&A, 137, L5 Leitherer, C. et al. 1999, ApJS, 123, 3 Lupton, R., Gunn, J. E., Ivezić, Z., Knapp, G. R., & Kent, S. 2001, in Astronomical Society of the Pacific Conference Series, Vol. 238 Astronomical Data Analysis Software and Systems X, ed. F. R. Harnden Jr., F. A. Primini, & H. E. Payne, 269 Madden, S. C., Galliano, F., Jones, A. P., & Sauvage, M. 2006, A&A, 446, Maller, A. H., Berlind, A. A., Blanton, M. R., & Hogg, D. W. 2009, ApJ, 691, 394 Maraston, C. 2005, MNRAS, 362, 799 Martin, D. C. et al. 2005, ApJ, 619, L1 Masters, K. L., Giovanelli, R., & Haynes, M. P. 2003, AJ, 126, 158 Masters, K. L. et al. 2010, MNRAS, 404, 792 Mediavilla, E., Muñoz, J. A., Kochanek, C. S., Falco, E. E., Arribas, S., &

Motta, V. 2005, ApJ, 619, 749

Morrissey, P. et al. 2007, ApJS, 173, 682

ArXiv:0902.4240

Ménard, B., Scranton, R., Fukugita, M., & Richards, G. 2009,

Meurer, G. R., Heckman, T. M., & Calzetti, D. 1999, ApJ, 521, 64

Motta, V., Mediavilla, E., Muñoz, J. A., Falco, E., Kochanek, C. S., Arribas, S., García-Lorenzo, B., Oscoz, A., & Serra-Ricart, M. 2002, ApJ, 574, 719

Muñoz-Mateos, J. C. et al. 2009, ApJ, 701, 1965

Natta, A. & Panagia, N. 1984, ApJ, 287, 228

Noll, S. et al. 2009, A&A, 499, 69

O'Dowd, M. J. et al. 2009, ApJ, 705, 885

Oke, J. B. & Gunn, J. E. 1983, ApJ, 266, 713

Panuzzo, P., Granato, G. L., Buat, V., Inoue, A. K., Silva, L., Iglesias-Páramo, J., & Bressan, A. 2007, MNRAS, 375, 640

Pei, Y. C. 1992, ApJ, 395, 130

Pierini, D., Gordon, K. D., Witt, A. N., & Madsen, G. J. 2004, ApJ, 617, 1022

Reddy, N. A., Erb, D. K., Pettini, M., Steidel, C. C., & Shapley, A. E. 2010, ApJ, 712, 1070

Reddy, N. A., Steidel, C. C., Fadda, D., Yan, L., Pettini, M., Shapley, A. E., Erb, D. K., & Adelberger, K. L. 2006, ApJ, 644, 792

Salim, S. et al. 2007, ApJS, 173, 267

—. 2009, ApJ, 700, 161

Schlegel, D. J., Finkbeiner, D. P., & Davis, M. 1998, ApJ, 500, 525

Sersic, J. L. 1968, Atlas de galaxias australes (Cordoba, Argentina:

Observatorio Astronomico, 1968)

Silva, L., Granato, G. L., Bressan, A., & Danese, L. 1998, ApJ, 509, 103

Smith, J. D. T. et al. 2007, ApJ, 656, 770

Stecher, T. P. 1965, ApJ, 142, 1683 Stone, R. C. 1991, AJ, 102, 333

Stratta, G., Maiolino, R., Fiore, F., & D'Elia, V. 2007, ApJ, 661, L9

Takeuchi, T. T. et al. 2010, A&A, 514, A4+

Thilker, D. A. et al. 2007, ApJS, 173, 538

Tojeiro, R., Wilkins, S., Heavens, A. F., Panter, B., & Jimenez, R. 2009, ApJS, 185, 1 Tremonti, C. A. et al. 2004, ApJ, 613, 898

Trumpler, R. J. 1930, PASP, 42, 214

Tuffs, R. J., Popescu, C. C., Völk, H. J., Kylafis, N. D., & Dopita, M. A. 2004, A&A, 419, 821

Unterborn, C. T. & Ryden, B. S. 2008, ApJ, 687, 976

Városi, F. & Dwek, E. 1999, ApJ, 523, 265

Vázquez, G. A. & Leitherer, C. 2005, ApJ, 621, 695

Voit, G. M. 1992, MNRAS, 258, 841

Wang, B. & Heckman, T. M. 1996, ApJ, 457, 645

Wang, J., Hall, P. B., Ge, J., Li, A., & Schneider, D. P. 2004, ApJ, 609, 589

Wang, R. et al. 2008, ApJ, 687, 848

Weingartner, J. C. & Draine, B. T. 2001, ApJ, 548, 296

Werk, J. K. et al. 2010, AJ, 139, 279

Williams, R. J., Quadri, R. F., Franx, M., van Dokkum, P., & Labbé, I. 2009, ApJ, 691, 1879

Witt, A. N. & Gordon, K. D. 1996, ApJ, 463, 681

-. 2000, ApJ, 528, 799

Witt, A. N., Thronson, Jr., H. A., & Capuano, Jr., J. M. 1992, ApJ, 393, 611

Xilouris, E. M., Byun, Y. I., Kylafis, N. D., Paleologou, E. V., & Papamastorakis, J. 1999, A&A, 344, 868

Xu, C. & Buat, V. 1995, A&A, 293, L65

Yip, C., Szalay, A. S., Wyse, R. F. G., Dobos, L., Budavári, T., & Csabai, I. 2010, ApJ, 709, 780

York, D. G. et al. 2000, AJ, 120, 1579

—. 2006, MNRAS, 367, 945

Zaritsky, D. 1994, AJ, 108, 1619

Zubko, V., Dwek, E., & Arendt, R. G. 2004, ApJS, 152, 211

APPENDIX

THE MILKY WAY EXTINCTION CURVE FOR ARBITRARY UV BUMP STRENGTH

In this Appendix, we provide formulae to construct an extinction curve analogous to the average MW extinction curve, but for arbitrary UV bump strength. We adopt the Cardelli et al. (1989) parameterization of the MW extinction and only modify their formulae where necessary. Below, B will be the single parameter characterizing the strength of the UV bump at 2175Å. A value of B = 0.0 results in no UV bump, while a value of B = 1.0 returns the standard MW UV bump strength. An IDL routine that computes the extinction curve for arbitrary R_V and B is available upon request from the authors.

Cardelli et al. parameterize the MW extinction curve in the following way:

$$A(\lambda)/A_V = a(x) + b(x)/R,\tag{A1}$$

where x has units of μm^{-1} , $R \equiv E(B-V)/A_V$, $A(\lambda)$ is the wavelength-dependent extinction in magnitudes, A_V is the extinction in the V-band, and a(x) and b(x) are specified in the following piece-wise continuous way:

In the infrared: $0.3\mu m^{-1} < x < 1.1\mu m^{-1}$,

$$a(x) = 0.574x^{1.61}$$
, (A2)

$$b(x) = -0.527x^{1.61}. (A3)$$

In the optical/near–IR: $1.1 \mu m^{-1} < x < 3.3 \mu m^{-1}$ and $y \equiv x - 1.82$,

$$a(x) = 1 + 0.177 y - 0.504 y^{2} - 0.0243 y^{3} + 0.721 y^{4} + 0.0198 y^{5} - 0.775 y^{6} + 0.330 y^{7},$$
(A4)

$$b(x) = 1.413 y + 2.283 y^{2} + 1.072 y^{3} - 5.384 y^{4} - 0.622 y^{5} + 5.303 y^{6} - 2.090 y^{7}.$$
 (A5)

In the near/mid–UV: $3.3 \mu m^{-1} < x < 5.9 \mu m^{-1}$,

$$f_a = \left(\frac{3.3}{x}\right)^6 (-0.0370 + 0.0469B - 0.601B/R + 0.542/R),\tag{A6}$$

$$a(x) = 1.752 - 0.316x - \frac{0.104B}{(x - 4.67)^2 + 0.341} + f_a,$$
(A7)

$$b(x) = -3.09 + 1.825x + \frac{1.206B}{(x - 4.62)^2 + 0.263}.$$
 (A8)

In the far–UV: $5.9 \mu m^{-1} < x < 8.0 \mu m^{-1}$,

$$f_a = -0.0447(x-5.9)^2 - 0.00978(x-5.9)^3$$
, (A9)

$$f_b = 0.213(x-5.9)^2 + 0.121(x-5.9)^3,$$
 (A10)

$$a(x) = 1.752 - 0.316x - \frac{0.104B}{(x - 4.67)^2 + 0.341} + f_a,$$
(A11)

$$a(x) = 1.752 - 0.316x - \frac{0.104B}{(x - 4.67)^2 + 0.341} + f_a,$$

$$b(x) = -3.09 + 1.825x + \frac{1.206B}{(x - 4.62)^2 + 0.263} + f_b.$$
(A11)